Front. Chem. Sci. Eng. 2025, 19(6): 49
https://doi.org/10.1007/s11705-025-2550-5

RESEARCH ARTICLE

Chitosan complex based hybrid material as catalyst for hydrogen evolution reaction

A. V. Khramenkova (✉)[1], D. N. Izvarina[1], V. V. Moshchenko[1], V. A. Smoliy[1], L. V. Klimova[1], O. E. Polozhentsev[2], A. N. Kuznetsov[3], K. M. Popov[4]

1 Platov South-Russian State Polytechnic University (NPI), Novocherkassk 346428, Russia
2 The Smart Materials Research Institute, Southern Federal University, Rostov-on-Don 344090, Russia
3 Boreskov Institute of Catalysis, Siberian Branch of the Russian Academy of Sciences, Novosibirsk 630090, Russia
4 Nikolaev Institute of Inorganic Chemistry, Siberian Branch of the Russian Academy of Sciences, Novosibirsk 630090, Russia

Abstract The hybrid material based on polyelectrolyte complexes of chitosan with oxycompounds of cobalt and nickel was electrodeposited on a stainless steel plate using the method of non-stationary electrolysis. The hybrid material layer was investigated by scanning electron microscopy, atomic force microscopy, transmission electron microscopy, X-ray diffraction, X-ray photoelectron spectroscopy, Brunauer-Emmett-Teller method, Fourier transform infrared spectroscopy, and Raman spectroscopy. The electrocatalytic properties of the hybrid material were studied in the hydrogen evolution reaction in alkaline electrolyte (1 mol·L^{-1} NaOH). It was determined that during the initial four-hour period of the hydrogen evolution process, the overpotential underwent a substantial decline, remaining constant for a minimum of 17 h thereafter, from 289 up to 210 mV at −10 mA·cm^{-2}. After a long-term hydrogen evolution, the activity of the hybrid material electrode exceeded hydrogen evolution reaction activity by 20% Pt/C commercial catalyst at a high current density of −100 mA·cm^{-2}.

Keywords chitosan polyelectrolyte complexes, cobalt hydroxide, nickel hydroxide, catalyst, hydrogen evolution reaction, non-stationary electrolysis

1 Introduction

The necessity to develop new materials has been driven by the rapid advancements in the field of hydrogen energy. The issue of developing new catalysts for electrochemical hydrogen evolution is a pressing one [1−3]. The high cost of platinum metal-based catalysts, despite their efficiency, has prompted a shift in research focus toward the development of new non-platinum catalysts for the hydrogen evolution reaction (HER), which must be characterized by structural stability and sufficiently fast reaction kinetics. One of the objectives of this research is to reduce the cost of electrolytic hydrogen [4,5].

For the above purposes, the synthesis of hybrid electrocatalysts based on the polymers and metal nanoparticles or their oxides seems promising [6]. Such electrocatalysts must have high specific surface area and pore volume, low cost, and generally contribute to high hydrogen spillover kinetics [7]. It is important to note that the presence of the organic component in such hybrid material (HM)—conducting polymers with an amorphous phase—contributes to the structural stability of hybrid catalysts and provides higher hydrophilicity, allowing mass transfer and hydrogen flow at sufficiently high current densities [8].

The coordination polymers/metal-organic frameworks (MOF) are of great interest among the hybrid HER catalysts, which have a number of advantages over other types of such materials due to their synergistic catalytic effect [9]. Thus, the authors [10] synthesized chemically a series of organometallic framework compounds with the general formula Fe_2-M-MOF (M = Fe, Co, Ni, Zn, Mn, L = 3,3,5,5′-azoxybenzenetetracarboxylic acid). The Fe_2-Co-MOF electrocatalysts exhibited high activity in HER in 0.1 mol·L^{-1} KOH solution with an over potential of 339 mV at a current density of 10 mA·cm^{-2}.

It is evident that the development of efficient electrocatalysts based on hybrid materials for HER and small organic molecule oxidation reactions is of significant interest and importance [11,12]. It is important to acknowledge the significance of binder-free hybrid

Received January 14, 2025; accepted March 21, 2025;
online April 25, 2025

E-mail: anna.vl7@yandex.ru

electrocatalysts that are positioned on the surface of a solid support. The presence of a polymer binder has the potential to impede the mass transfer process, which is a crucial aspect for the catalysis reaction [13]. In turn, the preparation of this binder-free hybrid electrocatalysts requires the development of new directed methods for their synthesis.

Previously, we have shown the prospects of using the method of non-stationary electrolysis for the synthesis of HM based on polyelectrolyte complexes of chitosan with oxycompounds of cobalt and nickel on the stainless steel surface AISI 304 [14]. The aim of this work is to study the physical-chemical and electrocatalytic properties of the prepared hybrid material.

2 Experimental

The electrolyte for deposition of the HM was prepared as described in our previous work [14]. Electrolyte solutions were prepared from chemically pure reagents in distilled water.

AISI 304 stainless steel macroelectrodes were used as work electrode. Prior to the deposition of the hybrid material, the surface of the steel support underwent a treatment involving abrasive (corundum) and chemical degreasing in an alkaline electrolyte. Counter electrode was nickel. The materials contained therein are as follows: cobalt nitrate ($Co(NO_3)_2 \cdot 6H_2O$), nickel chloride and nickel nitrate ($NiCl_2 \cdot 6H_2O$ and $Ni(NO_3)_2 \cdot 6H_2O$, respectively), poly-epichlorohydrin-dimethylamine (polyECHDMA), and chitosan. We used food grade chitosan (Bioprogress, Shchelkovo, Russia), a surfactant polyECHDMA (MBI Sintez, Volzhskii, Russia), and metal salts (LenReaktiv, St. Petersburg, Russia).

The formation of the hybrid material was carried out on a pretreated surface of a stainless steel plate under the action of an asymmetrical alternating current of industrial frequency, representing two half sine waves of different amplitudes. The ratio of the amplitudes of the cathode (I_k) and anode (I_a) currents averaged over the period was 2.0:1.65; electrolysis temperature was 30–40 °C; pH 2–3, electrolysis time 60 min.

To prepare the electrolyte, a weighed portion of chitosan was dissolved in 1 $mol \cdot L^{-1}$ HCl solution in the first beaker. In the second beaker, the solution containing cobalt nitrate ($Co(NO_3)_2 \cdot 6H_2O$), nickel chloride and nitrate ($NiCl_2 \cdot 6H_2O$ and $Ni(NO_3)_2 \cdot 6H_2O$, respectively) was prepared, and the surfactant poly-epichlorohydrin-dimethylamine was added. The resulting solution was stirred with a magnetic stirrer for thirty min. Both solutions were then mixed and stirred for one hour.

2.1 Material characterization

The morphology of the hybrid material was studied using a Quanta 200 scanning electron microscope. To determine the wetting angle, a sample of the hybrid material was placed on a table with adjustable height, and a 3 μL drop of distilled water was applied using a micropipette. The specimen was illuminated from one side by a lamp, and a camera was positioned opposite the specimen and imaged using DSA1 v1.9 software. The calculation of wetting angles was conducted automatically, employing the tangent method. The surface morphology of the hybrid material on the stainless steel surface was investigated using a Solver HV high vacuum scanning probe microscope: vacuum mode-natural environment, NSG20 probe sensor, data acquisition technique- semi-contact. The morphology and chemical composition of the HM electrodes was studied using a Hitachi Regulus SU8230 FESEM scanning electron microscope (Hitachi, Tokyo, Japan) with an accelerating voltage of 2 and 5 kV in the modes of secondary and backscattered electrons using an upper detector, which makes it possible to obtain microscopic images in phase and topographic contrasts. The surface morphology of the HM was also studied using high-resolution transmission electron microscopy (HRTEM), ThemisZ electron microscope (Thermo Fisher Scientific, USA) with an accelerating voltage of 200 kV and a limiting resolution of 0.07 nm. The images were recorded using a Ceta 16 CCD sensor (Thermo Fisher Scientific). The device is equipped with a SuperX (Thermo Fisher Scientific) energy-dispersive characteristic X-ray spectrometer (EDX) with a semiconductor Si detector with an energy resolution of 128 eV. The samples were ultrasonically dispersed onto perforated carbon substrates attached to copper grids.

The phase composition was studied using a transmission electron microscope (TEM) Zeiss Libra 200FE (Carl Zeiss) at an accelerating voltage of 200 kV. The values of the interplane distances d_{hkl} from the diffraction pattern were calculated using the formula: $d_{hkl}(m) = (\lambda(m))/R(m) \cdot 10^{-3} \cdot K^{-1}$, where R(m) is the radius of the reflexes circles, λ(m) is the wavelength of electrons, K is the calibration coefficient. The 200 kV voltage corresponds to the radius of the reflex circles $\lambda^{-1} = 398.7\ nm^{-1}$ and the electron wavelength λ = 2.508 pm. Calibration was carried out using polycrystalline aluminum foil (Agar Scientific Ltd.).

The X-ray diffraction (XRD) in transmission mode was studied using MoKα radiation (λ = 0.7093 Å) on a STOE STADI MP instrument (STOE, Germany) using MYTHEN2 1K detector. The 2θ range from 2° to 32° was scanned with a step of 0.015°. The average size of the coherent scattering region of the crystalline phases was determined from the peak broadening using the Scherrer equation, taking into account the instrumental broadening measured from the X-ray diffraction pattern of the NIST SRM 660c (LaB6) reference sample.

The device is equipped with an AztecLive (Oxford

Instruments, Oxford, UK) energy-dispersive X-ray characteristic spectrometer with a semiconductor Si detector with an energy resolution of 128 eV.

The low temperature Brunauer-Emmett-Teller (BET) method on "ASAP 2020" instrument was applied to determine the specific surface area of the hybrid material. A hybrid material sample was placed in the measuring cuvette of the surface area and porosity analyzer; the mass difference between the cuvette with the sample and the empty cuvette helped to determine the mass of the suspended sample placed in the cuvette. The sample was then degassed at 35 °C for 12 h at a pressure of less than 0.5 mmHg. Following the process of degassing, the sample was reweighed in order to compensate for the alteration in mass that had occurred. A cuvette containing a degassed sample of the hybrid material was then placed in the analysis port of a specific surface area and porosity analyzer to determine the specific surface area of the samples by physical adsorption of nitrogen onto the sample surface at 77 K. The measurements were performed automatically.

X-ray photoelectron spectra (XPS) were obtained on a SPECS electron spectrometer with FOIBOS-150 (SPECS) energy analyzer using non-monochromatized MgKα and AlKα radiation. The optical spectra in the fourier transform infrared (FTIR) area were measured on the laboratory infrared Fourier spectrometer Vertex 70 (Bruker) in the range of 50–5000 cm^{-1}, standard spectral resolution is 0.5 cm^{-1}. Raman spectra were obtained on a Horiba-Jobin Yvon Labram300 spectrometer equipped with a microscope with a spatial resolution of 5 μm. The spectral resolution of the instrument was 1.5 cm^{-1}. The excitation line of the CR spectrum was used as the excitation line of a 633 nm He-Ne laser with a wavelength of 633 nm and a power of 1.5 mW.

Electrochemical impedance spectroscopy (EIS) measurements were performed on a biologic SP-300 Potentiostat (Bio-Logic Science Instrument). The EIS spectra were recorded at 0 V versus Ag/AgCl (3.5 $mol \cdot L^{-1}$ KCl) reference electrode with an amplitude of 5 mV from 100000 to 0.01 Hz in a three-electrode cell. EC-laboratory app was used for EIS spectra fitting.

2.2 Investigation of the electrocatalytic properties of hybrid materials

Electrochemical measurements were carried out in a three-electrode homemade Teflon cell at room temperature (~25 °C) in 1 $mol \cdot L^{-1}$ NaOH electrolyte under Ar atmosphere. The counter electrode (Ni foam with high surface area) compartment was separated from the working electrode compartment by Nafion membrane, and the reference electrode (commercial (Biologic, France) mercury oxide electrode Hg/HgO 1 $mol \cdot L^{-1}$ NaOH) was placed into the working electrode compartment. The potential and current were controlled using a PS-50 potentiostat (Smart-Stat, Russia); all electrode potentials reported in this paper are referred to the reversible hydrogen electrode (RHE) ($E_{Hg/HgO}$ = + 0.930 V *vs*. RHE).

The working electrode was utilized in its prepared state, with no additional treatments being applied. The cell is filled with supporting electrolyte 1 $mol \cdot L^{-1}$ NaOH. The electrolyte in both compartments of the cell was purged with argon gas for at least 20 min prior to measurement. Cyclic voltammetry curves were recorded first in the range from –0.060 to 0.400 V (RHE) with a sweep rate of 20 $mV \cdot s^{-1}$, then the measurements were performed in the potential range required to determine the characteristics of the electrode.

To ascertain the catalytic activity of the HM material in the hydrogen evolution reaction, the working electrode was initially "trained" through cycling of potential in the range of –0.100 to 0.030 V at a sweep rate of 10 $mV \cdot s^{-1}$ for a minimum of 10 cycles. Subsequently, the active resistance of the electrochemical system was measured by impedance spectroscopy to further correct the working electrode potential (iR compensation). HER cyclic voltammetry (CV) curve was recorded in the range of iR-corrected potentials from 0.030 V to E_{cathod} (to achieve current density of –100 $mA \cdot cm^{-2}$) at sweep rate of 5 $mV \cdot s^{-1}$ (at least two cycles). The iR-correction of potential was done automatically by Smart-Stat soft used 85% of the measured impedance. All currents were normalized on a geometric surface area of the working electrode.

3 Results and discussion

The morphology of the HM films prepared on the stainless steel support was investigated by scanning electron microscopy (SEM) and atomic force microscopy (AFM). The surface of the HM layer is smooth with fissures. The formation of polyelectrolyte complexes of chitosan results in the establishment of a polymer network, the HM layer being non-uniform in height (Fig. 1(a)). The difference in thickness of the HM layer can be achieved up to 1.2 μm (Figs. 1(c) and 1(d)). The similar topography of chitosan-based layers was observed earlier in work [15].

It is known that the more hydrophilic the electrode surface is, the higher the adsorption ability for water (electrolyte) or OH^- intermediates, which can effectively accelerate the Volmer step in the HER process [16]. The contact wetting angle of the synthesized films was measured to be 67 degrees, thus indicating their hydrophilic properties (Fig. 1(b)).

It can be seen from the TEM image (Fig. 2(a)) that the substance of the HM represents the agglomerates of particles, and the interplanar distances of 1.33, 1.53, and

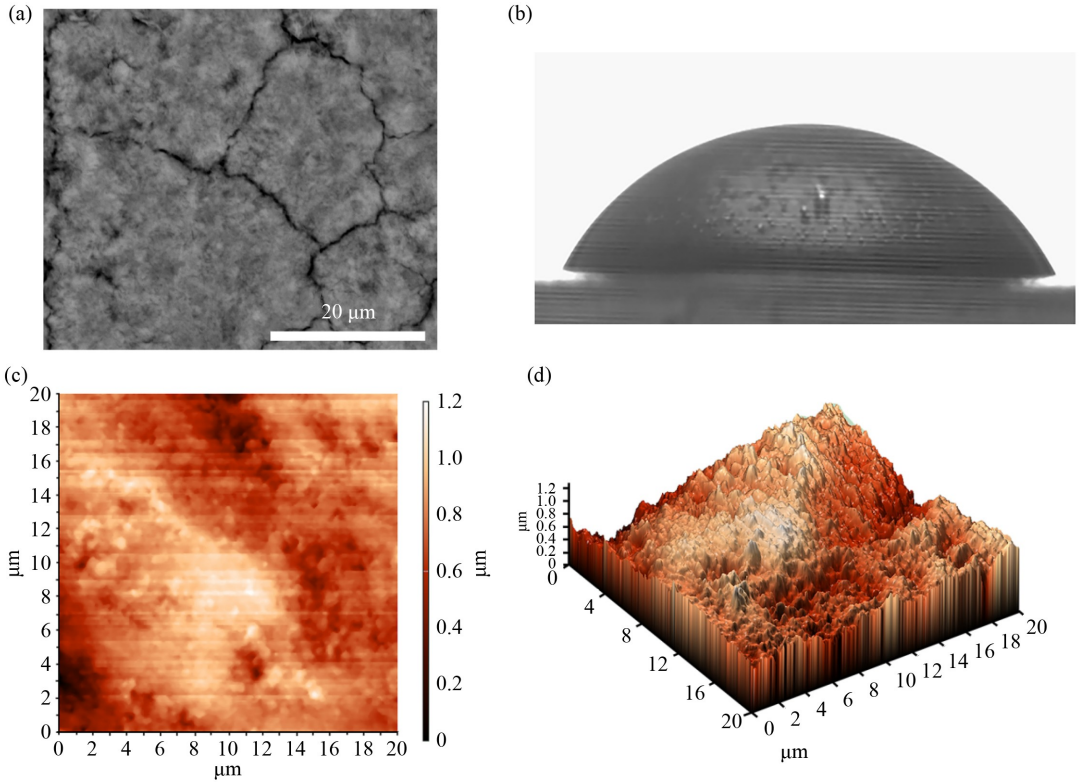

Fig. 1 (a) SEM-image of the HM surface; (b) photograph of a water drop on the HM surface; (c, d) AFM image of the HM surface.

2.67 Å are determined by SAED correspond to chitosan. We found that the main phase of the HM, according to XRD is the cobalt hydroxyisocyanate phase $Co(OCN)_{0.6}(OH)_{1.4}(H_2O)_{0.6}$ ($P6_3/mmc$, z = 2) (PDF card No. 04-015-5621) (Fig. 2(b)), the jamborite phase ($Ni(OH)_2$(NiOOH)) (PDF#01-089-7111 a = b = 3.071 Å; c = 23.2 Å) and $Ni(OH)_2 \cdot 0.75H_2O$ (PDF#00-038-0715 a = b = 3.08 Å; c = 23.41 Å) (Fig. 2(c)). The reflections are shifted toward smaller angles compared to the original sample, which indicates a significant increase in the crystal lattice parameters (up to a = b = 3.10 Å; c = 23.70 Å). The average size of the crystallites (D_{XRD}) was estimated as 14.0 nm. As demonstrated in Fig. 2(d), the HM adsorption isotherm can be classified as type IV according to the Brunauer, Deming, and Teller classification. This is supported by the relatively minor increase in the amount of sorbed nitrogen in the initial part of the isotherm, as well as the data presented in Table 1, which indicates the predominant presence of mesoporous. The isotherm also displays the presence of a hysteresis loop, which corresponds to type H3 according to the IUPAC classification. This is a characteristic feature of adsorbents with slit-like pores or those composed of plane-parallel particles.

As illustrated by the Raman spectrum (Fig. 2(e)), a pronounced, highly polarized peak at 518 cm^{-1} is evident. This peak can be ascribed to the lattice vibrations of $Co(OH)_2$ [17]. A shoulder at 456 cm^{-1} is also observed in this spectrum, corresponding to the strain mode of OCoO [18]. Another shoulder at 647 cm^{-1} is also seen in the above Raman spectrum, which may correspond to the polymorphic modification of CoO(OH). Furthermore, the Raman spectrum shows the characteristic peaks of the chitosan functional groups. For example, a low-intense peak at 395 cm^{-1} corresponds to δ(C–C(=O)–C), at 1035 cm^{-1} to δ(C–H) [19], and a broad band at 1287 cm^{-1} may correspond to $\delta(CH_2)$, δ(CH), and δ(OH) vibrations [20].

Comparative analysis of the FTIR spectra of pure chitosan (Fig. 2(f)) and HM was carried out earlier in [14] and also indicates the occurrence of complex formation processes. Figure 3 shows HRTEM images of the hybrid material at different magnification (Figs. 3(a)–3(c)), high-angle annular dark field (HAADF) scanning transmission electron microscopy (STEM) image (Fig. 3(d)) and EDX mapping (Figs. 3(e)–3(h)) of the HM. As can be seen, the HM consists of thin homogeneous extended plates with a large lattice distance of ca. 0.6717 nm. These are the organo-metallic layers, which transform into the oxide phases when exposed to a radiation beam (Fig. 3(c), left area of the image). EDX mapping data show that characteristic signals from Co, Ni, and O are observed in the HM substance. Cobalt and nickel are uniformly distributed in the organo-metallic plates of the HM. The separated clusters of Co and Ni were not observed.

We provided the detailed description of XPS spectra of the hybrid materials in our previous studies [14]. Moreover, it should be noted that the lines of chlorine, oxygen, nitrogen, carbon, nickel, and cobalt spectra are observed on the survey spectrum (Fig. 4(a)). The peaks

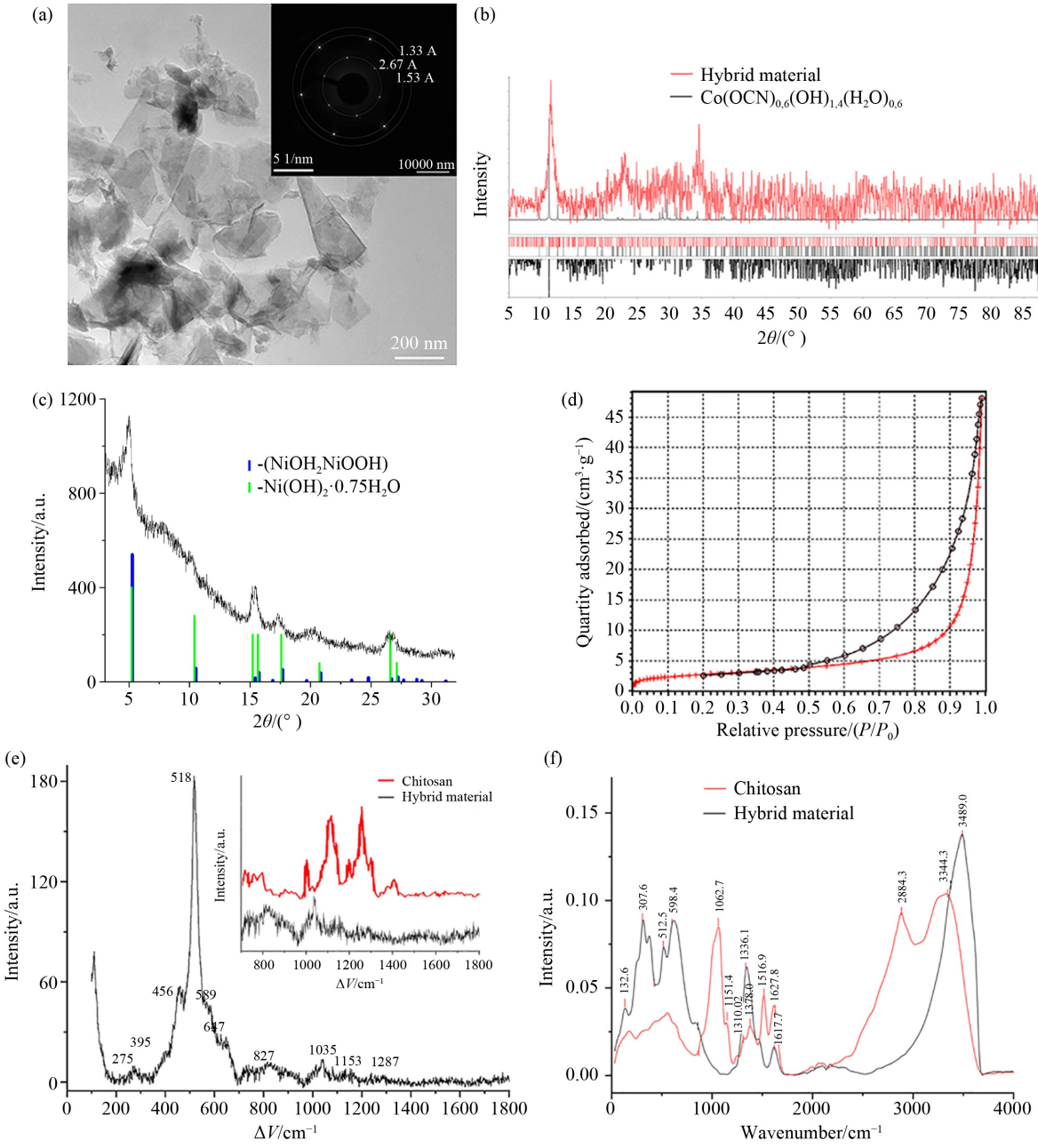

Fig. 2 (a) TEM-image of the HM corresponding SAED patterns; (b, c) XRD diffraction pattern of the HM; (d) N_2 adsorption/desorption isotherm of HM; (e) Raman spectra of HM. The inset shows a part of Raman spectra of the HM compared to spectra of pure chitosan; (f) IR absorption spectra.

Table 1 Results of calculation micropores specific surface area and volume by *t*-plot

Specific surface per micropore, $S_{sp.micro.}/(m^2 \cdot g^{-1})$	$(S_{sp.micro.}/S_{sp.})$/ %	Specific volume of micropores, $V_{sp.micro.}/(cm^3 \cdot g^{-1})$	Correlation coefficient, *r*
0.887	8.89	0.000329	0.9999

on the spectrum of C 1s correspond to C–C/C–C–H, C–O, and C=O groups (Fig. 4(b)). XPS data are also in line with the results outlined above (Fig. 4(c)). The O 1s spectrum (Fig. 4(c)) displays that oxygen is in the composition of the complex compound. The nitrogen spectrum displays three discernible components, attributable to the presence of nitrogen in three distinct crystal chemical positions (Fig. 4(d)). There is a single peak on Cl 2p spectra (Fig. 4(e)) indicating the presence of chlorine in +1 charge state. The Ni 2p and Co 2p spectrums (Fig. 4(f) and 4(g) correspondingly) display that both nickel and cobalt are mainly in +2 charge state. It has been established that the state of films composed of hybrid materials is subject to alteration during

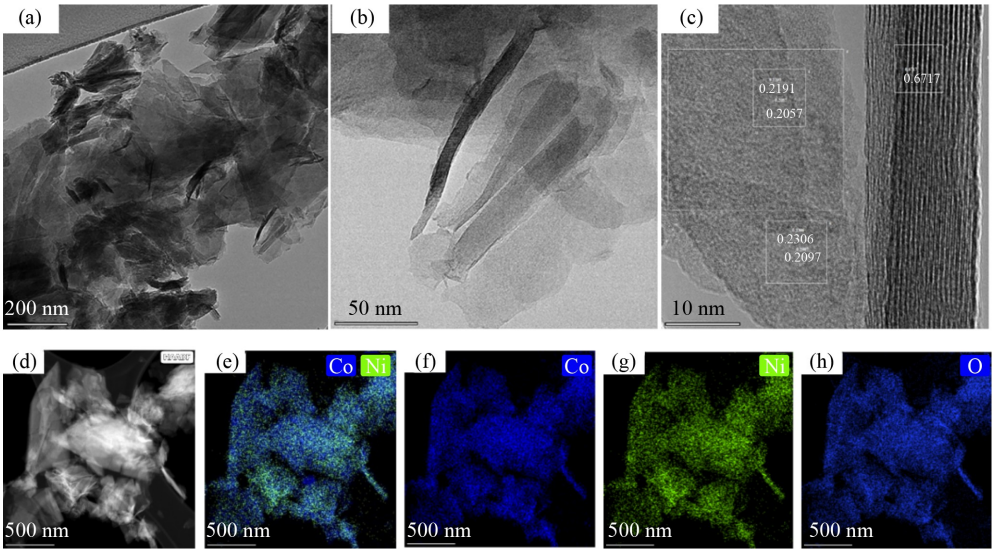

Fig. 3 (a–c) HRTEM images of the HM, (d) HAADF-STEM image, and (e–h) EDX mapping of the HM.

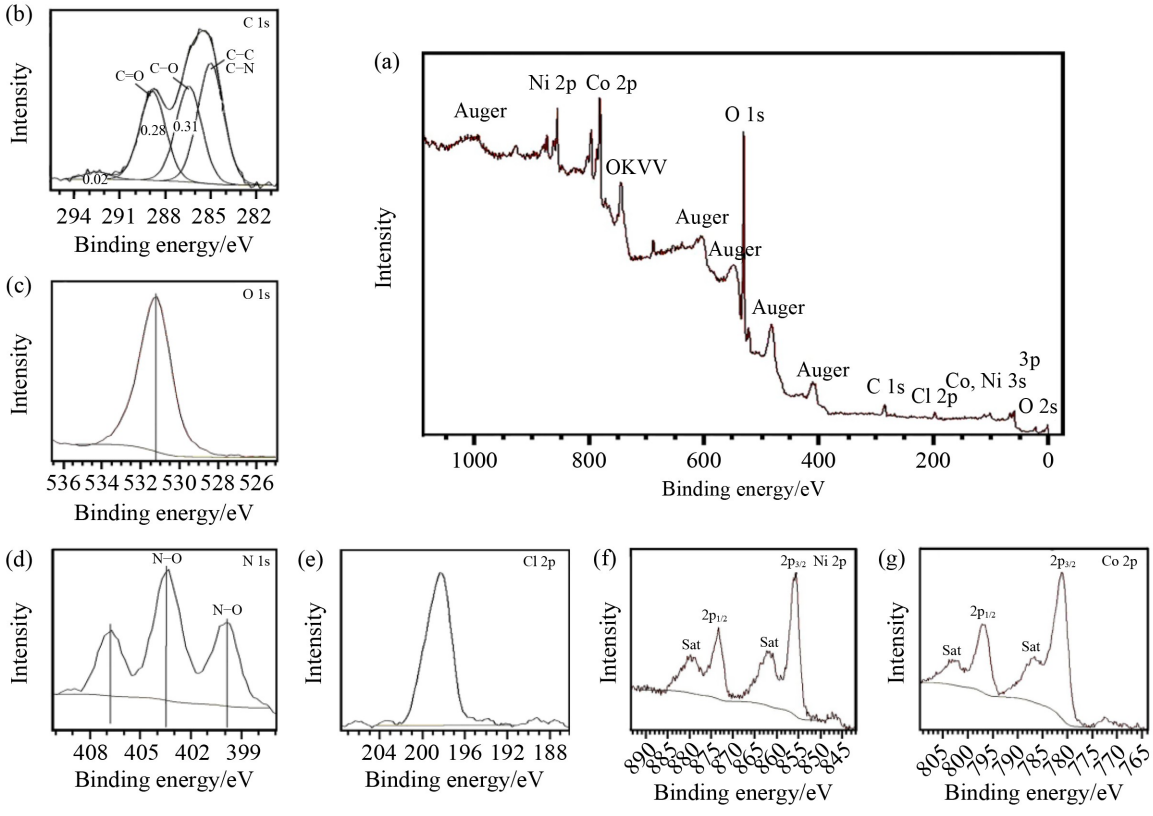

Fig. 4 XPS spectra of hybrid material: (a) survey spectrum, (b) C 1s, (c) O 1s, (d) N 1s, (e) Cl 2p, (f) Ni 2p, (g) Co 2p.

electrochemical processes at the phase interface. The impedance measurements (complex resistance for alternating current) were conducted to facilitate a more comprehensive identification of the characteristics of the synthesized hybrid materials and their electrical properties.

To assess the contribution of chitosan and its effect on the electrochemical properties of hybrid materials in general, studies were conducted on the electrochemical impedance spectra of both hybrid materials, pure chitosan, and a film on the surface of stainless steel obtained from the developed electrolyte in the absence of chitosan. Impedance spectra were taken in the frequency range of 100 kHz to 0.01 Hz using 5 mV small amplitude alternating signal (Fig. 5). As demonstrated in Fig. 5, a distinct semicircle is evident in the high and medium frequencies of the impedance spectrum for a film derived from a developed electrolyte in the absence of chitosan.

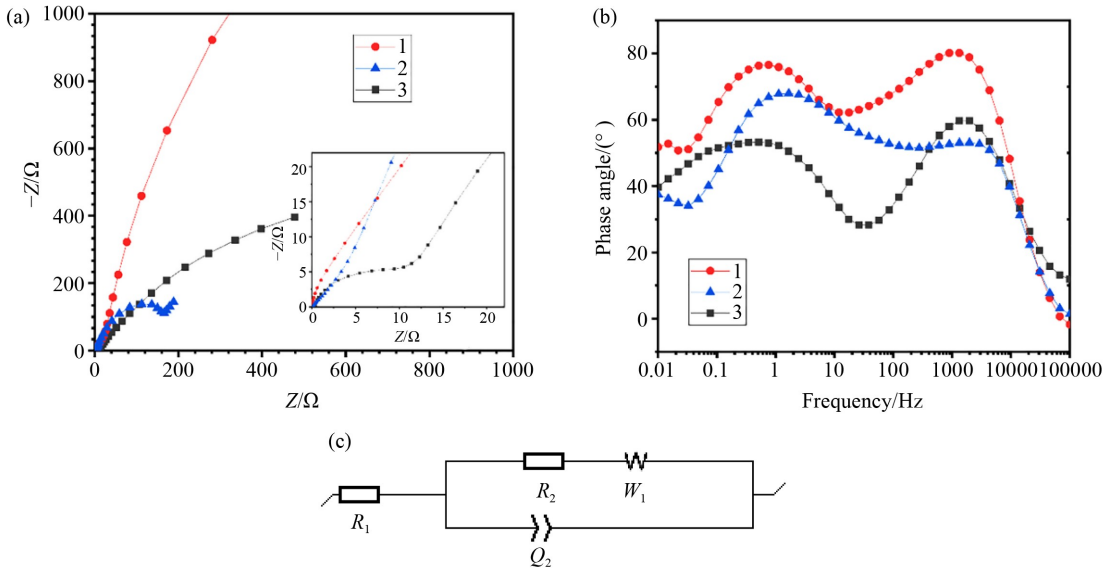

Fig. 5 Electrochemical impedance spectroscopy data: (a) Nyquist diagrams, (b) Bode plot of EIS spectra, and (c) equivalent electrical circuit. (1) A pure chitosan film, (2) a hybrid material, and (3) a film obtained from a developed electrolyte in the absence of chitosan.

Meanwhile, smaller semicircles are observed on the spectra of pure chitosan and hybrid material, which is probably due to less charge transfer resistance at the interface. At the same time, the analysis of impedance spectra in the films under scrutiny reveals the occurrence of semicircles, succeeded by inclined curves situated within the low frequency range. The resulting impedance spectra were analyzed using EC-laboratory software based on an equivalent electrical circuit (Fig. 5(c), Table 2), which provides information on ion diffusion and charge transfer processes of the electrodes under study. When crossing the X axis in the high-frequency region, the internal resistance (R_1) can be determined. This resistance encompasses not only the electrolyte resistance but also the transition resistance of the material under investigation, specifically the current collector. The charge transfer resistance at the interface (R_2) associated with the Faraday processes can be determined from the diameter of the semicircle. The oblique line in the region of lower frequencies (of the order of 26 Hz) is at an angle between 45° and 90° to the X axis (Fig. 5(a)), which can be explained by the diffusion of the electrolyte deep into the electrode and fitted by the Warburg element W [21]. An additional constant phase element Q_2 was added to the circuit in parallel with R_2 to describe the electrical dispersions in the real electrode.

A comparison of the parameters of the equivalent impedance circuit (Table 2) reveals that the resistance R_1 of the hybrid material is approximately three times less than that of the film obtained from the developed electrolyte in the absence of chitosan, and is comparable to the resistance of the pure chitosan film. The R_2 resistance of the hybrid material is also lower than that of a film made from the developed electrolyte in the absence of chitosan. The decline in resistance R_1 may be attributed

Table 2 Comparison of equivalent impedance circuit parameters

Sample	R_1/Ω	R_2/Ω	$\sigma_w/(\Omega\cdot s^{-1/2})$	$Q_2/(F\cdot s^{(a_2-1)})$	a_2
Film in the absence of chitosan	0.3468	8.684	62.44	1.55e–04	0.8879
Chitosan film	0.1036	7.424	276.7	1.33e–04	1
Hybrid material	0.1091	2.581	122	2.102e–03	0.7511

to the enhanced conductivity of the hybrid material, attributable to the incorporation of chitosan in its composition. The decrease in R_2 resistance may be due to the improvement in the capacitive behavior of the electrode by increasing the diffusion of electrolyte ions, which reduces the charge resistance at the interface. To consider the low frequency region, the Bode plot of EIS spectra (Fig. 5(b)) is observed, where a higher maximum phase angle value of ~68° for the hybrid material is noted when compared to a film obtained from the developed electrolyte in the absence of chitosan, which has a value of ~53°. This is associated with a higher capacitive behavior of the hybrid material in the low frequency region. The analysis of the results obtained allows the conclusion to be drawn that the inclusion of chitosan in the composition of the film of oxygen-containing compounds of cobalt and nickel leads to a change in the nature of conductivity and results in higher conductivity values of the hybrid material compared to the film obtained in the absence of chitosan.

The prepared electrode with the HM layer was investigated by electrochemical methods and in HER in alkaline electrolyte. Comparative characteristics of the electrocatalytic properties of the developed HM are shown in Fig. 6 and Table 3. Figure 6 shows HER CV curves for the HM electrode (initial and after stability test) and for comparison, 60% Ni/C and 20% Pt/C catalysts. The HER activity (the value of overpotential at

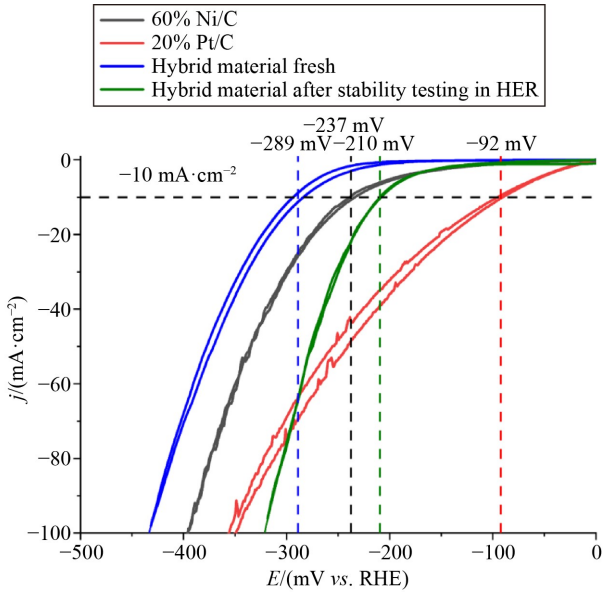

Fig. 6 CV curves of hydrogen evolution reaction recorded for the fresh prepared and after stability test HM electrodes, 60% Ni/C and 20% Pt/C catalysts (1 mol·L^{-1} NaOH, sweep rate 5 mV·s^{-1}).

–10 mA·cm^{-2}) of the HM electrode increased significantly after the stability test. That exceeded noticeably the activity of 60% Ni/C catalyst. It is interesting to note that the difference in overpotentials between HM electrode (after stability test) and Pt/C catalyst at –10 mA·cm^{-2} is less than 120 mV. And the HM layer is more active in HER than Pt/C at a current density of –100 mA·cm^{-2}. Thus, the prepared HM is promising as a catalyst for the HER in alkaline electrolyte. The findings of this study are consistent with the data from previous research, e.g [25,26].

It is important to note that the presence of an organic component of hybrid materials—preferably conducting polymers with an amorphous phase—contributes to the structural stability of hybrid catalysts. Furthermore, it provides a higher hydrophilicity that promotes mass transfer and the hydrogen evolution reaction at sufficiently high current densities. The synergetic effect of Co and Ni hydroxides and chitosan allows water adsorption/dissociation to occur on a surface with much lower potential energy [27]. Moreover, the synergistic effect has been demonstrated to enhance the electrocatalytic activity of the electrode, thereby reducing the overpotential for HER.

Tafel plots for the HM electrodes, including Ni/C and Pt/C catalysts, are presented in Fig. 7 to assess the HER kinetics. The resulting Tafel plot of Pt/C is 30 mV·dec^{-1}, suggesting that HER pathways follow the Volmer-Tafel mechanism with discharging of two H_{ads} as the rate-determining step (RDS), Tafel step-chemical desorption. Tafel plots of Ni/C and the HM electrodes (fresh and after HER) are 140, 78, and 110 mV·dec^{-1}, respectively, that indicates that the HER process might follow the Volmer-Heyrovsky mechanism, and the Volmer reaction is the RDS.

The CV curves of the HER were recorded at two distinct temporal points: prior to and following the stability test. The stability test was performed in 1 mol·L^{-1} NaOH in galvanostatic mode at a current density of –10 mA·cm$^{-2}_{geom}$, for 21 h (Fig. 8(a)). To demonstrate clearly the catalytic properties of the HM, the bare stainless steel support was tested in a stability experiment under the same conditions.

Figure 8 shows the change of HER overpotential in time at –10 mA·cm^{-2} for the HM electrode and the bare stainless steel support. The overpotential undergoes a decline during the initial four-hour period, subsequently reaching a state of equilibrium. It is important to note that HER also occurs on the stainless steel electrode, but at much higher values of overpotential, that directly indicates the catalytic effect of the HM layer. The observed decrease in the overpotential of HER for the HM electrode, or alternatively the increase in HM electrode activity in HER, can be attributed to the reduction of metal oxides (nickel and cobalt) in the HM layer. The CV curves of the HM electrode recorded in 1 mol·L^{-1} NaOH both prior to and following the stability test demonstrate a significant increase in current. Concurrently, a clearly expressed reversible peak from oxidation/reduction of nickel and/or cobalt oxides emerges (Fig. 8(b)). That is due to the development of electrochemically available surface of active components of the HM layer.

The long-term stability test of the HM electrode in HER at –100 mA·cm^{-2} was performed. Figure 9 shows the value of overpotential decreases during the initial five- to ten-hour period, and then it remains almost constant. The observed overpotential surges are attributable to the presence of hydrogen bubbles on the

Table 3 Comparative characteristics of the developed HM as electrocatalysts for hydrogen evolution

Electrode material	Current density/(mA·cm^{-2})	Potential/mV	Electrolyte	Ref.
$Co_{0.85}Se$ hollow nanospheres anchored on N-doped graphene nanosheets	–10	–227	1 mol·L^{-1} KOH	[22]
Ni- and Co-substituted metallic MoS_2	–10	–240	1 mol·L^{-1} KOH	[23]
Ni- Co nanocomposites deposited on carbon fiber paper	–10	–313	1 mol·L^{-1} KOH	[24]
Catalyst 60% Ni/KB600	–10	–237	1 mol·L^{-1} NaOH	This work
Hybrid material based on polyelectrolyte complexes of chitosan	–10	–210	1 mol·L^{-1} NaOH	This work
Commercial catalyst 20% Pt/Vulcan	–10	–92	1 mol·L^{-1} NaOH	This work

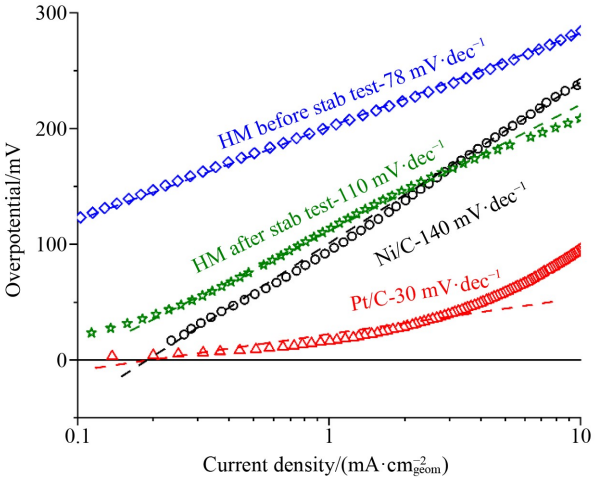

Fig. 7 Tafel plots for the HM electrodes, Ni/C, and Pt/C catalysts.

surface of the working electrode. The same test was carried out for the commercial Pt/C catalyst, but after 42 h it was stopped due to the fast increase in the overpotential. Figures 10(a) and 10(f) show the digital image of the HM electrodes before and after 140 h of hydrogen evolution. The HM layer changed the color from green-blue to olive. It has some voids that means the part of active layer was detached during the HER. A detailed study was performed using SEM with EDX mapping to analyze the HM electrodes both in their original state and following a long-term stability test in HER. HM electrode in its original state has a smooth active layer which dense covers the stainless-steel support (Fig. 10(b)). The layer consists of Co and Ni (hydro-) oxides thin structures fixed on the stainless-steel with an organic matrix (Fig. 10(c)). The weight ratio of Co and Ni in the fresh catalytic layer is 3:1 (Fig. 10(d)). After long-term stability test (140 h) in the hydrogen evolution, the hybrid material layer has more developed cracks and voids (Fig. 10(f)). The thin structure of Co and Ni (hydro-) oxides was found to change into thicker plates (some of which exhibited a hexagonal form) that were interconnected to each other (Fig. 10(g)). The HM layer consists of less organic matrix, especially, inside the voids, where CoO*x* structures are predominant. The weight ratio of Co and Ni in the catalytic layer after test in HER is 1.75:1 (Fig. 10(h)). A detailed study of the nature of stable hybrid material layer with a focus on the kinetics of its evolution during the hydrogen reaction is in progress. The findings of this study will be presented in a forthcoming publication.

4 Conclusions

The hybrid material, which is based on the polyelectrolyte complexes of chitosan with oxycompounds of cobalt and nickel on a stainless steel surface, was prepared using the method of non-stationary electrolysis. The prepared material was characterized by SEM, AFM, TEM, XRD, XPS, BET, IR, and Raman spectroscopy in detail. The HM layer has smooth morphology with a difference in height up to 1.2 μm.

Electrochemical properties of the HM were studied both in supporting electrolyte, 1 mol·L^{-1} NaOH, and in the HER. The broad peak observed in the cyclic voltammetry curves can be attributed to reversible oxidation/reduction processes involving oxycompounds of cobalt and nickel. The fresh prepared HM demonstrated moderate activity in the HER—overpotential of 289 mV at –10 mA·cm^{-2}. However, the HER overpotential demonstrated a significant decline during the initial four-hour stability test, maintaining a constant level for a minimum of 17 h thereafter, up to the value of 210 mV at –10 mA·cm^{-2}. This HM (after stability test) exceeded 60% Ni/C catalyst at –10 mA·cm^{-2} and 20% Pt/C commercial catalyst at high current density of –100 mA·cm^{-2}.

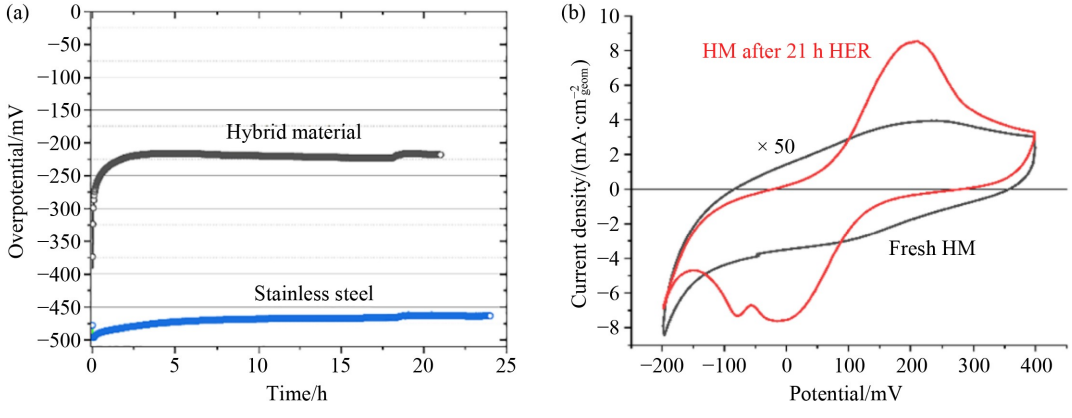

Fig. 8 (a) Dependence of overpotential in time of hydrogen evolution reaction in long-term stability test of the HM electrode and bare stainless-steel support in 1 mol·L^{-1} NaOH electrolyte, current density –10 mA·cm^{-2}; (b) CV curves of the fresh prepared HM electrode (black) and the HM electrode after stability testing in HER (red). Current density for fresh HM is increased 50 times for clarity (1 mol·L^{-1} NaOH electrolyte, sweep rate 20 mV·s^{-1}).

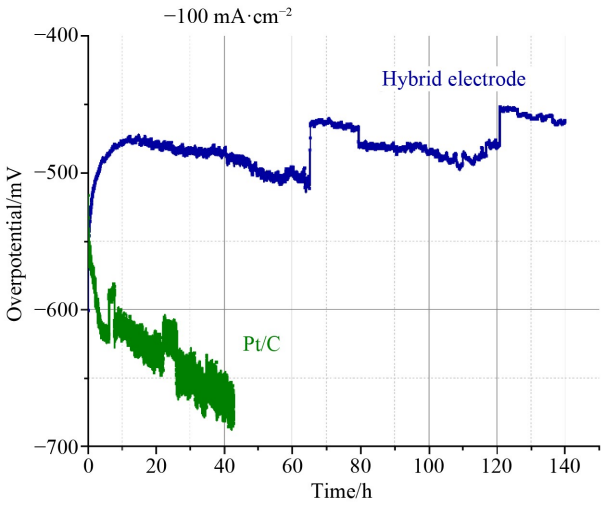

Fig. 9 The long-term stability test of the HM electrode and commercial Pt/C catalyst in HER at –100 mA·cm^{-2} (electrolyte 1 mol·L^{-1} NaOH).

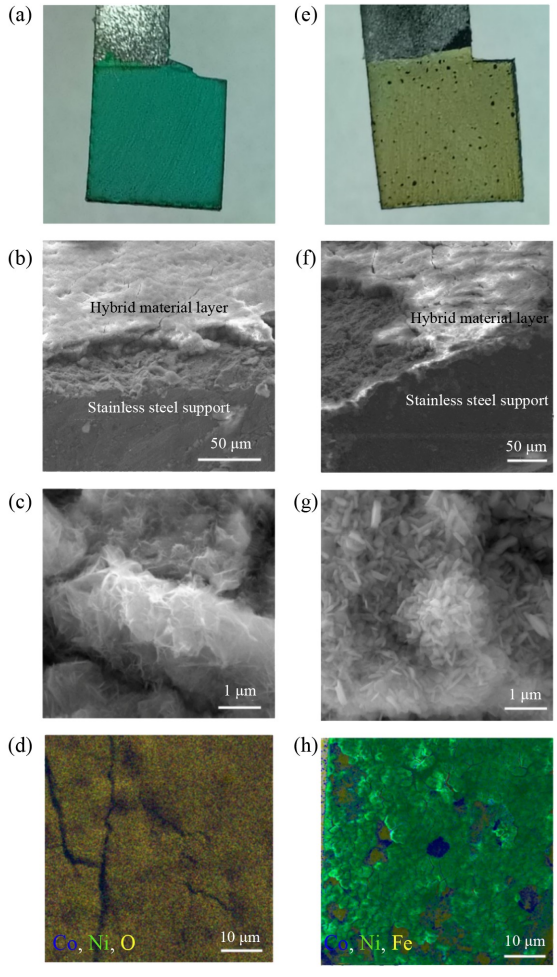

Fig. 10 (a–d) Digital photo, SEM images, and EDX mapping as-prepared and (e–h) after stability test in HER at –100 mA·cm^{-2}.

Consequently, the HM, derived from the polyelectrolyte complexes of chitosan with oxycompounds of cobalt and nickel, is a promising catalytic material for the HER. A forthcoming detailed study of the HM following its stabilization in a long-term hydrogen evolution test is anticipated to enhance its catalytic properties.

Competing interests The authors declare that they have no competing interests.

Acknowledgements This work was supported by the Ministry of Science and Higher Education of the Russian Federation within the governmental assignment for Boreskov Institute of Catalysis (Project No. FWUR-2024-0036) (A. N. Kuznetsov). This work was supported by the Ministry of Science and Higher Education of the Russian Federation (Project No. 121031700314-5) (K. M. Popov). The experiments were carried out using facilities of the shared research center National Center of Investigation of Catalysts at Boreskov Institute of Catalysis. The experiments were carried out using facilities of the shared research center Center for Physical and Physicochemical Methods of Analysis, Study of Properties and Characteristics of Surfaces, Nanostructures, Materials and Products UdmFRC UB RAS, Shared Use Center Nanotechnologies, Platov South-Russian State Polytechnic University (NPI).

References

1. Pu Z, Amiinu I S, Zhang C, Wang M, Kou Z, Mu S. Phytic acid-derivative transition metal phosphides encapsulated in N, P-codoped carbon: an efficient and durable hydrogen evolution electrocatalyst in a wide pH range. Nanoscale, 2017, 9(10): 3555–3560
2. Pu Z, Cheng R, Zhao J, Hu Z, Li C, Li W, Wang P, Amiinu I S, Wang Z, Wang M, et al. Anion-modulated platinum for high-performance multifunctional electrocatalysis toward HER, HOR, and ORR. iScience, 2020, 23(12): 101793
3. Pu Z, Liu T, Amiinu I S, Cheng R, Wang P, Zhang C, Ji P, Hu W, Liu J, Mu S. Transition-metal phosphides: activity origin, energy-related electrocatalysis applications, and synthetic strategies. Advanced Functional Materials, 2020, 30(45): 2004009
4. Lv J, Wang Z, Miura H. The effects of ball milling on microstructures of graphene/Ni composites and their catalytic activity for hydrogen evolution reaction. Materials Letters, 2017, 206: 124–127
5. Mollamahale Y B, Jafari N, Hosseini D. Electrodeposited Ni-W nanoparticles: enhanced catalytic activity toward hydrogen evolution reaction in acidic media. Materials Letters, 2018, 213: 15–18
6. Chakrabartty S, Gopinath C S, Raj C R. Polymer-based hybrid catalyst of low Pt content for electrochemical hydrogen evolution. International Journal of Hydrogen Energy, 2017, 42(36): 22821–22829
7. Kousar N, Sannegowda L K. Hybrid cobalt phthalocyanine polymer as a potential electrocatalyst for hydrogen evolution reaction. International Journal of Hydrogen Energy, 2024, 50: 37–47
8. Zhao S, Yin L, Deng L, Song J, Chang Y M, Hu F, Wang H, Chen H Y, Li L, Peng S. Inheritable organic-inorganic hybrid interfaces with π-d electron coupling for robust electrocatalytic hydrogen evolution at high-current-densities. Advanced

Functional Materials, 2023, 33(6): 2211576

9. Sundriyal S, Kaur H, Bhardwaj S K, Mishra S, Kim K H, Deep A. Metal-organic frameworks and their composites as efficient electrodes for supercapacitor applications. Coordination Chemistry Reviews, 2018, 369: 15–38
10. Gu M, Wang S C, Chen C, Xiong D, Yi F Y. Iron-based metal–organic framework system as an efficient bifunctional electrocatalyst for oxygen evolution and hydrogen evolution reactions. Inorganic Chemistry, 2020, 59(9): 6078–6086
11. Giddaerappa K N, Deshpande U, Sannegowda L K. Cobalt phthalocyanine based metal-organic framework as an efficient bifunctional electrocatalyst for water electrolysis. Energy & Fuels, 2024, 38(9): 8249–8261
12. Patil G, Daniel S, Lokesh K S. Tuning the active sites of polymeric palladium phthalocyanine with Ketjen black for robust hydrogen evolution. International Journal of Hydrogen Energy, 2024, 86: 104–113
13. Cai J, Liao X, Li P, Wang Q, Huang H, Lyu Z, Lin J, Xie S. Penta-twinned Rh@ Pt core-shell nanobranches with engineered shell thickness for reversible and active hydrogen redox electrocatalysis. Chemical Engineering Journal, 2022, 429: 132414
14. Khramenkova A V, Izvarina D N, Popov K M, Khimich M A, Litovchenko I Yu. A novel hybrid electrode materials for supercapacitors based on polyelectrolyte chitosan complex. Solid State Ionics, 2023, 403: 116385
15. Bardetsky D, Zhitomirsky I. Electrochemical preparation of composite films containing cationic polyelectrolytes and cobalt hydroxide. Surface Engineering, 2005, 21: 125–130
16. Li Q, Huang F, Li S, Zhang H, Yu X Y. Oxygen vacancy engineering synergistic with surface hydrophilicity modification of hollow Ru doped CoNi-LDH nanotube arrays for boosting hydrogen evolution. Small, 2022, 18(2): 2104323
17. Oyedotun K O, Masikhwa T M, Mirghni A A, Mutuma B K, Manyala N. Electrochemical properties of asymmetric supercapacitor based on optimized carbon-based nickel-cobalt-manganese ternary hydroxide and sulphur-doped carbonized iron-polyaniline electrodes. Electrochimica Acta, 2020, 334: 135610
18. Yang J, Liu H, Martens W N, Frost R L. Synthesis and characterization of cobalt hydroxide, cobalt oxyhydroxide, and cobalt oxide nanodiscs. Journal of Physical Chemistry C, 2010, 114(1): 111–119
19. Ren X D, Liu Q S, Feng H, Yin X Y. The characterization of chitosan nanoparticles by Raman spectroscopy. Applied Mechanics and Materials, 2014, 665: 367–370
20. Lapo B, Demey H, Carchi T, Sastre A M. Antimony removal from water by a chitosan-iron(III)[ChiFer(III)] biocomposite. Polymers, 2019, 11(2): 351
21. Aguilera L, Aguiar P C M, Ruiz Y L, Almeida A, Moreira J A, Passos R R, Pocrifka L A. Electrochemical synthesis of γ-CoOOH films from α-$Co(OH)_2$ with a high electrochemical performance for energy storage device applications. Journal of Materials Science: Materials in Electronics, 2020, 31(4): 3084–3091
22. Wang H, Wang X, Yang D, Zheng B, Chen Y. $Co_{0.85}Se$ hollow nanospheres anchored on N-doped graphene nanosheets as highly efficient, nonprecious electrocatalyst for hydrogen evolution reaction in both acid and alkaline media. Journal of Power Sources, 2018, 400: 232–241
23. Attanayake N H, Dheer L, Thenuwara A C, Abeyweera S C, Collins C, Waghmare U V, Strongin D R. Ni-and Co-substituted metallic MoS_2 for the alkaline hydrogen evolution reaction. ChemElectroChem, 2020, 7(17): 3606–3615
24. Gorospe A E G B, Balela M D L. Ni-Co nanocomposites deposited on carbon fiber paper as an electrocatalyst towards hydrogen evolution reaction. Materials Today: Proceedings, 2020, 22: 255–261
25. Tiwari J N, Sultan S, Myung C W, Yoon T, Li N, Ha M, Harzandi A M, Park H J, Kim D Y, Chandrasekaran S S, et al. Multicomponent electrocatalyst with ultralow Pt loading and high hydrogen evolution activity. Nature Energy, 2018, 3(9): 773–782
26. Wang Q, Xu C Q, Liu W, Hung S F, Yang H B, Gao J, Cai W, Chen H M, Li J, Liu B. Coordination engineering of iridium nanocluster bifunctional electrocatalyst for highly efficient and pH-universal overall water splitting. Nature Communications, 2020, 11: 4246
27. Lv Z, Wang M, Liu D, Jian K, Zhang R, Dang J. Synergetic effect of Ni_2P and MXene enhances catalytic activity in the hydrogen evolution reaction. Inorganic Chemistry, 2021, 60(3): 1604–1611